Energy & Environmental Science

ROYAL SOCIETY OF CHEMISTRY

PAPER

View Article Online
View Journal | View Issue

Cite this: *Energy Environ. Sci.*, 2023, **16**, 1620

A 5 V-class cobalt-free battery cathode with high loading enabled by dry coating†

Weiliang Yao, [a] Mehdi Chouchane,[b] Weikang Li, [c] Shuang Bai,[a] Zhao Liu,[d] Letian Li,[d] Alexander X. Chen, [c] Baharak Sayahpour,[a] Ryosuke Shimizu,[c] Ganesh Raghavendran,[c] Marshall A. Schroeder,[e] Yu-Ting Chen, [a] Darren H. S. Tan,[c] Bhagath Sreenarayanan,[c] Crystal K. Waters,[f] Allison Sichler,[f] Benjamin Gould,[f] Dennis J. Kountz,[f] Darren J. Lipomi, [c] Minghao Zhang*[c] and Ying Shirley Meng *[bc]

Transitioning toward more sustainable materials and manufacturing methods will be critical to continue supporting the rapidly expanding market for lithium-ion batteries. Meanwhile, energy storage applications are demanding higher power and energy densities than ever before, with aggressive performance targets like fast charging and greatly extended operating ranges and durations. Due to its high operating voltage and cobalt-free chemistry, the spinel-type $LiNi_{0.5}Mn_{1.5}O_4$ (LNMO) cathode material has attracted great interest as one of the few next-generation candidates capable of addressing this combination of challenges. However, severe capacity degradation and poor interphase stability have thus far impeded the practical application of LNMO. In this study, by leveraging a dry electrode coating process, we demonstrate LNMO electrodes with stable full cell operation (up to 68% after 1000 cycles) and ultra-high loading (up to 9.5 mA h cm^{-2} in half cells). This excellent cycling stability is ascribed to a stable cathode–electrolyte interphase, a highly distributed and interconnected electronic percolation network, and robust mechanical properties. High-quality images collected using plasma focused ion beam scanning electron microscopy (PFIB-SEM) provide additional insight into this behavior, with a complementary 2-D model illustrating how the electronic percolation network in the dry-coated electrodes more efficiently supports homogeneous electrochemical reaction pathways. These results strongly motivate that LNMO with a high voltage cobalt-free cathode chemistry combined with an energy-efficient dry electrode coating process opens up the possibility for sustainable electrode manufacturing using cost-effective and high-energy-density cathode materials.

Received 29th November 2022,
Accepted 14th February 2023

DOI: 10.1039/d2ee03840d

rsc.li/ees

Broader context

The mobile electronics revolution, mass adoption of electric vehicles, and increasing efforts to incorporate intermittent renewable energy sources into the grid underscore humanity's growing need for sustainable rechargeable batteries. Since their advent in 1991, Li-ion batteries (LIBs) have served as the workhorse technology for enabling these transitions, but the high cost, limited sustainability, poor safety, and fundamental performance limits of established cobalt-based Li-ion chemistries still impede broader adoption and technological capabilities. As one of the most promising next generation cobalt-free cathode materials, $LiNi_{0.5}Mn_{1.5}O_4$ (LNMO) is still facing challenges such as poor cycling stability. Here we present a dry-electrode strategy to enable LNMO at high areal loading up to a 9.5 mA h cm^{-2} level with robust mechanical properties, a homogeneous electronic percolation network and mitigated parasitic reactions. This method not only achieves stable long-term cycling but also removes toxic *N*-methyl-2-pyrrolidone (NMP) during the drying process, therefore providing an environmentally benign pathway for future high energy density and cost-effective LIB manufacturing.

[a] *Materials Science and Engineering, University of California San Diego, La Jolla, CA 92093, USA*
[b] *Pritzker School of Molecular Engineering, University of Chicago, Chicago, IL, 60637, USA. E-mail: shirleymeng@uchicago.edu*
[c] *Department of NanoEngineering, University of California San Diego, La Jolla, CA 92093, USA. E-mail: miz016@eng.ucsd.edu*
[d] *Materials and Structural Analysis, Thermo Fisher Scientific, 5350 NE Dawson Creek Drive, Hillsboro, Oregon 97124, USA*
[e] *Battery Science Branch, Energy Science Division, Army Research Directorate, DEVCOM Army Research Laboratory, Adelphi, MD 20783, USA*
[f] *Advanced Performance Materials Chemours Discovery Hub, The Chemours Company, Newark, DE 19713, USA*

† Electronic supplementary information (ESI) available. See DOI: https://doi.org/10.1039/d2ee03840d

Introduction

Reducing the content of cobalt in cathode materials is becoming a critical requirement for the next generation of Li-ion batteries (LIBs). The cost of the battery industry's reliance on cobalt is not only highly volatile from a commercial perspective (doubled to $80 000 USD per ton in one year[1]) due to strategic international stockpiling and the monopoly in supply from the Democratic Republic of Congo, but also raises severe ethical concerns with its mining and child labor.[2] Therefore, reducing or completely removing cobalt from cathode materials has become an urgent challenge to achieve environmentally benign and sustainable battery manufacturing. Among the candidates, cobalt-free $LiNi_{0.5}Mn_{1.5}O_4$ (LNMO) with its high operating voltage ($\sim$4.7 V) can reduce the number of cells for the battery pack system, thus providing higher volumetric energy density. Despite its high energy density and low cost, LNMO is still facing various commercialization challenges such as poor cycling stability and low electronic conductivity ($\sim 10^{-6}$ S cm^{-1}).[3–7]

Among the efforts to improve the performance of LNMO, developing novel electrolyte additives is the most common strategy to stabilize the interphase of both the cathode and the anode.[8–15] However, in full cells, most studies are limited to 200 cycles or use cathode loading lower than 20 mg cm^{-2}, making them incompatible for practical applications. Materials doping is another approach to stabilize the cathode electrolyte interphase (CEI) while mitigating the electrolyte corrosion.[16] Nevertheless, this approach has only achieved limited success and the addition of expensive transition metals will raise the cost. Another approach involves surface coatings, which aim to slow down the cathode surface degradation and prolong cell cycling[17,18] by providing a more robust CEI and preventing transition metal dissolution. Unfortunately, the cost and equipment required for scaling up this sophisticated synthesis process likely precludes high-throughput manufacturing.[19,20] Despite the wealth of research focused on improving the performance of LNMO, few studies have considered a thick electrode approach to achieve practical usage, *i.e.*, at least 3.0 mA h cm^{-2} ($\sim$21 mg cm^{-2}) per side to achieve around 300 W h kg^{-1} (Table S1, ESI†). In these cases, the works targeting practical loadings were limited by either a low cycle number (less than 300 cycles) or poor capacity utilization.[21–23]

To realize the full potential of LNMO, high loading must be achieved simultaneously with other modifications. Many fabrication strategies have been explored, including repeated coextrusion/assembly to create artificial channels to reduce tortuosity and improve the ionic flow,[24] dispersing single-walled carbon nanotubes (SWCNTs) to fabricate 800 μm electrodes,[25] utilizing novel binders such as polyacrylonitrile (PAN) to enable high loading,[21] and adjusting the solid content in water based slurry with carbon micro fibers (CMFs).[26] However, these methods are all slurry-based approaches and either involve very complex procedures or are limited to lab scale processing. Conventionally, *N*-methyl-2-pyrrolidone (NMP) is widely used as the mixing solvent due to its excellent chemical and thermal stability as well as its ability to dissolve the polyvinylidene fluoride (PVDF) binder, which offers high mechanical and electrochemical stability in cathode operation.[27,28] However, NMP's notorious toxicity and requirement of expensive solvent recycling equipment make the slurry-based fabrication process costly (>$5m for NMP solvent recovery equipment), more energy demanding, and less sustainable.[29]

Unlike the abovementioned slurry-based methods, fabrication using binder fibrillation is a dry process, where polytetrafluoroethylene (PTFE) is the widely used binder, with the first use in dry electrodes for LIBs reported in 1979.[30] In this process, PTFE particles are shear mixed to form adhesive fibrils which can closely bind both conductive carbon and active materials. The dry coating process has recently drawn interest through Maxwell Technologies reporting high long-term cycling performance in 10 A h pouch cells[31] and Tesla's announcement in 2020 of using dry electrodes in EV batteries in their future vehicles.[32] Compared to the slurry-based method, this dry process can easily fabricate roll-to-roll electrodes with extreme thicknesses and no cracks in the electrode.[33,34] More importantly, with no drying process, the dry electrode method saves 45% to 47% energy consumption and $\sim$20% total battery manufacturing cost compared to the slurry-based method.[20] To reach TW h level energy storage, low cost, less energy waste and reduced environmental pollution are key factors to achieve sustainable manufacturing. Fig. 1 summarizes both conventional slurry-based and novel dry electrode fabrication methods.

In this work, we utilize the binder fibrillation process to fabricate LNMO electrodes at high loadings (>3.0 mA h cm^{-2} level) and demonstrate the performance improvement of long-term cycling in the high voltage (>4.7 V) LIBs' application. With the combined experimental and modeling efforts, we pinpoint the underlying mechanism of performance improvement by using dry-coated LNMO electrodes in terms of reduced parasitic reactions, a highly distributed and interconnected electronic percolation network, and robust mechanical properties.

Results and discussion

Fabrication of dry electrodes at high loadings

Before electrode fabrication, we evaluated the stability of the inactive components such as the current collector, binder and conductive carbon under high voltage. Linear sweep voltammetry (LSV) and cyclic voltammetry (CV) testing on various components were carried out and the results are shown in Fig. S1 (ESI†). Interestingly the Super C65 (SC65) triggered more electrolyte decomposition than vapor-grown carbon fiber (VGCF), likely because of its higher specific surface area.

To investigate the quality of the thick electrodes, plasma focused ion beam (PFIB) was adopted to mill electrode cross-sections (Fig. S2, ESI†). Xe^+ based PFIB allows much faster milling on large volumes (350 μm × 100 μm × 30 μm) compared to conventional Ga^+ based FIB ($\sim$1 hour milling *versus* >12 hours milling). These cross sections revealed that the slurry-based LNMO using VGCF exhibits severe carbon agglomeration, indicating the conventional slurry mixing failed

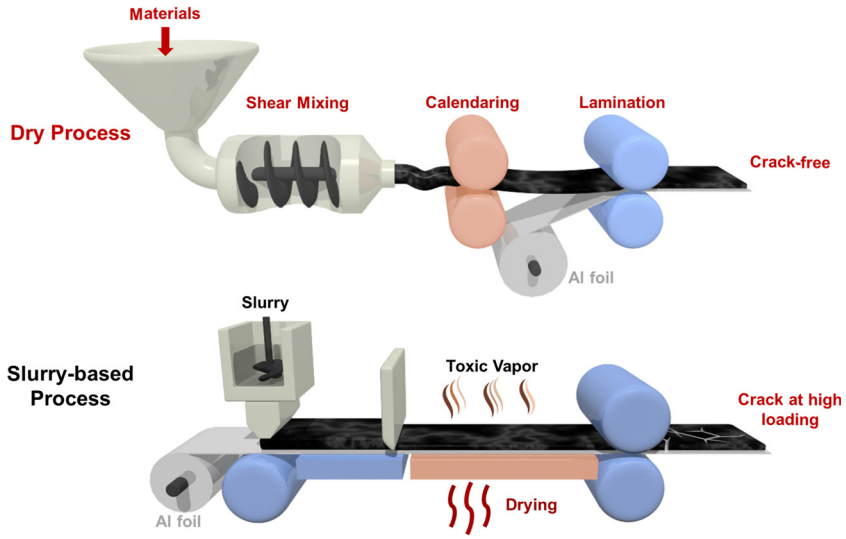

Fig. 1 Schematic of dry electrode and slurry-based cathode fabrication procedures.

to disperse the carbon fibers as uniformly as the SC65. Similar observations were also found on the top surface of these electrodes (Fig. S3, ESI†), indicating that the VGCF powder tends to aggregate into a group of fibers. Consequently, in slurry-based electrodes, most of the LNMO particles are not connected by VGCF, which severely hinders the electron flow from active materials to the current collector. This behavior is reflected by the poor cycling performance in the full cell for the slurry-based LNMO using VGCF (Fig. S4, ESI†). In contrast, the shear force applied during the dry process mixing straightens the fibers without breaking them to form a 'network'. The dry-LNMO full cell, which has a more homogeneous carbon distribution (Fig. S2A, ESI†), shows much more stable performance at both C/10 and C/3 rates. Interestingly, due to its nano-agglomerate morphology, the SC65 carbon in the dry electrode is unable to construct an effective electronic percolation network compared to VGCF, which has a similar fiber morphology to that of the fibrillated PTFE binder (Fig. S5, ESI†). Thus, this work will focus on the comparison between dry electrodes with VGCF and slurry-based electrodes with SC65.

Half cells were then fabricated to investigate the electrochemical performance. The dry electrodes, even with areal loadings as high as 9.5 mA h cm^{-2} ($\sim$240 μm), still delivered a similar performance to the baseline 3.0 mA h cm^{-2} level electrode (Fig. 2A and C). The slurry-based LNMO, however, starts to show obvious performance degradation at 4.0 mA h cm^{-2}, as seen from the increased polarization and capacity degradation in the voltage profiles (Fig. 2B and D). This impact is even more pronounced at higher areal loadings, as the 6.0 mA h cm^{-2} level slurry-based LNMO experienced severe electrode cracking after drying (Fig. S6, ESI†). In slurry-based electrodes at high areal loading, conductive carbon and binder will easily float near the electrode surface and agglomerate due to capillary action and diffusion.[35] This inhomogeneity in the conductive carbon distribution leads to a poor electronic percolation network, lowering the effective electronic conductivity further with electrode thickness. In contrast, for dry electrodes, both in-plane and out-of-plane electronic conductivities remain in the same order of magnitude as the areal loading is increased from 3 to 9.5 mA h cm^{-2} (Fig. S7, ESI†). This suggests that electron flow in both directions is well maintained even at an ultra-high loading, so the VGCF is likely well distributed. As a result, even at the 6.0 mA h cm^{-2} level, the dry-LNMO half cells can still deliver $>$110 mA h g^{-1} at a C/3 rate (Fig. S8A, ESI†), outperforming the 4.0 mA h cm^{-2} level slurry-based LNMO. With electrolyte which is compatible with the Li metal anode, the 6.0 mA h cm^{-2} level dry-LNMO can show a relatively stable cycling in 10 cycles (Fig. S8B, ESI†).

The mechanical behaviors of slurry-based and dry electrodes were then investigated using 90° peel and tensile (pull) tests (Fig. 2E and F). 90° peel tests (using scotch tape) were used to compare the debonding behavior of dry and slurry-based LNMO electrodes with the same areal loading (3.0 mA h cm^{-2}) and thicknesses ($\sim$90 μm). Fig. 2E compares the average thickness of each electrode removed during the peel test (*i.e.*, delaminated from the current collector and remaining on the adhesive tape) relative to the normalized peel-off force (normalized with the width of the tape). For slurry-based LNMO electrodes, on average, over half of the electrode was peeled off with less than 5.25 N m^{-1} force. In contrast, the dry-LNMO electrodes required more force ($\sim$4.20 to 14.70 N m^{-1}) to delaminate while removing less than half of the electrode thickness. Thus, more force was needed to delaminate less material for the dry-LNMO electrode in comparison to the slurry-based electrode. Likewise, the two types of electrodes differed in the manner by which they failed. Qualitatively, from Fig. S9A and B (ESI†), we observed that the dry-LNMO electrodes primarily experienced cohesive failure (*i.e.*, delamination within the electrode layer), while the slurry-based electrode experienced a mixture of both cohesive and adhesive (*i.e.*, delamination at the Al-electrode interface) failure. Together, these observations suggest that the dry-LNMO electrodes have better adhesion to the current collector, as well as greater cohesive strength within the electrode. This difference in adhesive and cohesive strength is

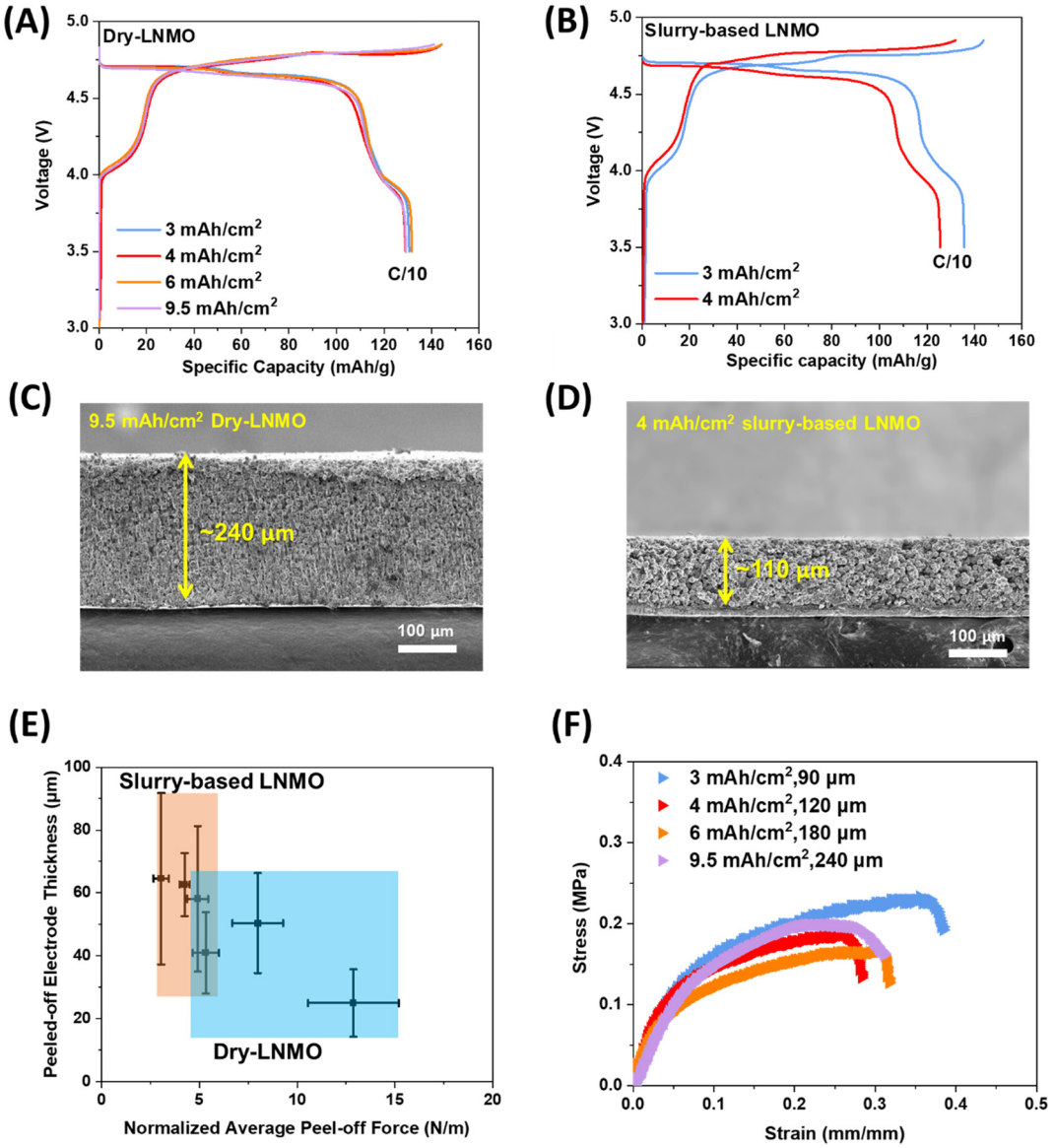

Fig. 2 Electrochemical and mechanical evaluation of high loading LNMO using both slurry-based and dry electrode methods. (A) Half-cell performance of dry-LNMO and (B) slurry-based LNMO at various areal loadings. SEM cross-sectional image of (C) 9.5 mA h cm^{-2} level dry-LNMO and (D) 4.0 mA h cm^{-2} level slurry-based LNMO. (E) Normalized peel-off forces and thickness of peeled-off electrodes from both dry-LNMO and slurry-based LNMO at an areal loading of 3.0 mA h cm^{-2}. (F) Representative stress–strain curves of dry electrodes with various areal loadings.

likely due to the morphology of the electrode stemming from the dry fabrication process. Dry-LNMO electrodes formed homogenously distributed PTFE fibrils, which help maintain the electrode structure (*e.g.*, dissipate mechanical energy) during mechanical failure. Likewise, the PTFE binder can take multiple forms, including nanofibrils (thickness ~20 nm, Fig. S10, ESI†) that can more effectively bind the LNMO and carbon fibers, further increasing the cohesive strength of the electrode. In comparison, the drying process of the slurry-based LNMO electrode results in phase segregation of the binder, carbon, and active materials, leading to uneven binder distribution. This phase segregation results in a concentration gradient where electrode layers closer to the current collector contain a lower concentration of the PVDF binder and layers further from the current collector contain a higher concentration.

The improved uniformity from the dry fabrication process is evident from the tensile behaviors of dry-LNMO electrodes with various areal loadings (Fig. 2F). Despite the significant increase in the thickness, the fracture behavior (Fig. S11, ESI†) and tensile properties of all electrodes remained similar, with tensile strengths ranging between 0.25–0.30 MPa and fracture strains between 18–26% (Fig. 2F and Table S3, ESI†). The vertical uniformity and robust mechanical properties of the dry electrodes help maintain a stable electrode structure from cell fabrication to long-term electrochemical cycling, thus providing fast electron transfer and reducing the cell impedance in the long run. More importantly, the removal of the solvent drying process significantly reduces energy consumption and eliminates the cost required to recover NMP, making the LIB

manufacturing process sustainable and more environmentally friendly.[36]

Modeling of the 2D electronic percolation network

To gain further insights from the PFIB-SEM cross-sectional images, a 2-D modeling approach has been developed, using a sub-volume of the extracted electrode as an input for the geometry. The two conditions that will be compared are the dry-LNMO with VGCF (Fig. 3A) and the slurry-based LNMO with SC65 (Fig. 3B), through a single discharge at a C-rate of C/3. The discussion over the fair comparison between these two slices and more details on the modeling effort such as the model description, and the parameters used are provided in the ESI.†

From the simulated discharge curves in Fig. 3C, the dry-LNMO displays a specific capacity of 125.2 mA h g^{-1} *versus* 101.6 mA h g^{-1} for the slurry-based LNMO. This difference is due to the higher overpotential in the slurry-LNMO, which will lead to a shorter discharge time before reaching the cut-off voltage of 3.5 V. On average, a potential difference of 0.24 V is observed for a given time of discharge between the slurry-based

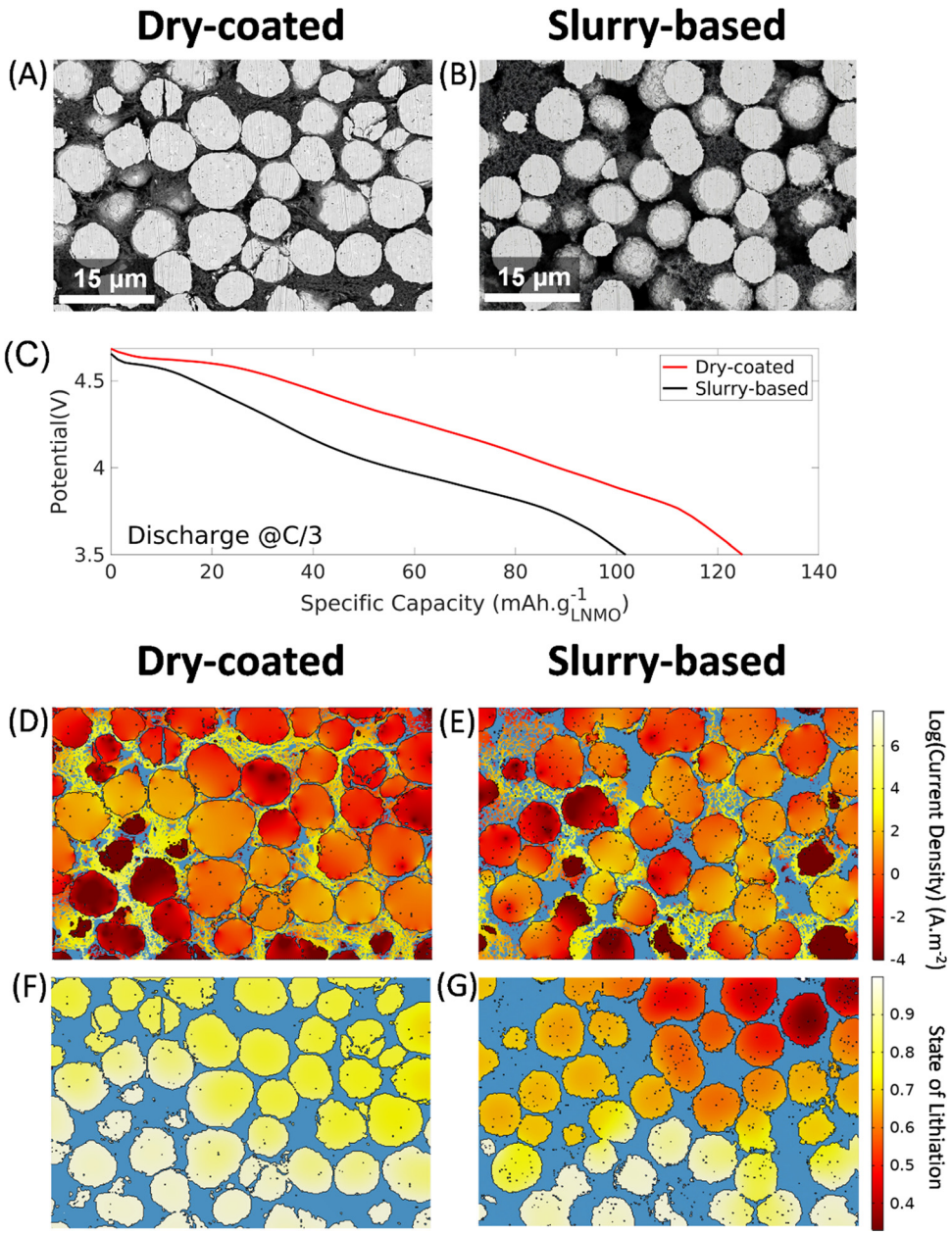

Fig. 3 2-D modeling results based on high-quality PFIB-SEM images. PFIB-SEM cross-sections of (A) dry coated and (B) slurry-based LNMO with SC65. (C) The simulated discharge curves for dry coated and slurry-based LNMO. Finally, the 2-D modeling results at the end of a discharge at C/3 are displayed with the current density in the solid phase and the state of lithiation reported for the dry coated LNMO, respectively, in (D and F), and for the slurry-based LNMO, respectively, in (E and G). The bottom of the electrodes corresponds to the current collector location and the top to the separator location in the simulations.

and dry-LNMO. To investigate the cause of this higher overpotential, the distribution of the log of the current density in the solid phase is plotted at the end of discharge in Fig. 3D and E. In the two electrodes, most of the current is flowing through the carbon network, which is the optimal scenario to prevent a significant ohmic drop due to the poor electronic conductivity of LNMO ($\sim 10^{-6}$ S cm^{-1}).[5] In the dry-LNMO shown in Fig. 3D, 99.62% of the current is flowing through the VGCF, while only 97.26% in the case of the slurry-based LNMO shown in Fig. 3E. This indicates a better connectivity of the VGCF network thanks to its fiber morphology compared to the SC65. In the slurry-based LNMO, the higher amount of current flowing through the LNMO will be detrimental to the performance of the battery, because it will induce a higher electronic resistivity, hence a higher voltage drop, entailing that the cut-off voltage will be reached sooner than previously observed.

This difference in electronic transport translates into the state of lithiation ($[Li]_{LNMO}/[Li]_{LNMO,max}$), with a more uniform and higher state of lithiation, *i.e.*, a better utilization, of the dry-LNMO (Fig. 3F) than the slurry-based LNMO with SC65 (Fig. 3G). It is noteworthy that the utilization is higher near the current collector than near the separator. This gradient is characteristic of a system limited by electronic transport, with poorly connected active material particles far from the current collector (the source of the electrons) having a lower state of lithiation. The absence of strong intraparticle gradients also demonstrates that the intercalation process is not limited by solid diffusion at this rate of discharge. Overall, through this modeling effort relying on high quality PFIB-SEM images, the efficiency of VGCF to form an electronic percolating network has been highlighted *versus* the reference case of SC65. Even though the model does not capture the long-term benefits from having VGCF (low surface carbon), that will hinder the side reactions when compared to SC65 (high surface carbon), it is still able to show its merits in terms of electronic conductivity.

Electrochemical performance and interfacial analysis

Long-term cycling performance using 3.0 mA h cm^{-2} LNMO electrodes was carried out with graphite as the counter electrode. The dry-LNMO full cell achieved 80% capacity retention after 300 cycles while slurry-based LNMO full cell only delivered 67% (Fig. 4A). Notably, the dry-LNMO full cell enables high coulombic efficiency (CE%) throughout the testing. The CE% increases to 99.9% after 115 cycles while the slurry-based LNMO full cell can only reach maximum $\sim$99.8% throughout the cycling. The slurry-based LNMO full cell shows a continuously growing overpotential while the overpotential of the dry-LNMO full cell is stabilized after 300 cycles (Fig. 4B). In addition, the oxidative peaks from the slurry-based LNMO full cell are found to shift more towards the higher voltage end, with a significant increasing trend in both redox peaks around 4.52 V (Ni^{2+}/Ni^{3+}) and 4.7 V (Ni^{3+}/Ni^{4+}) (Fig. S15A and B, ESI†).

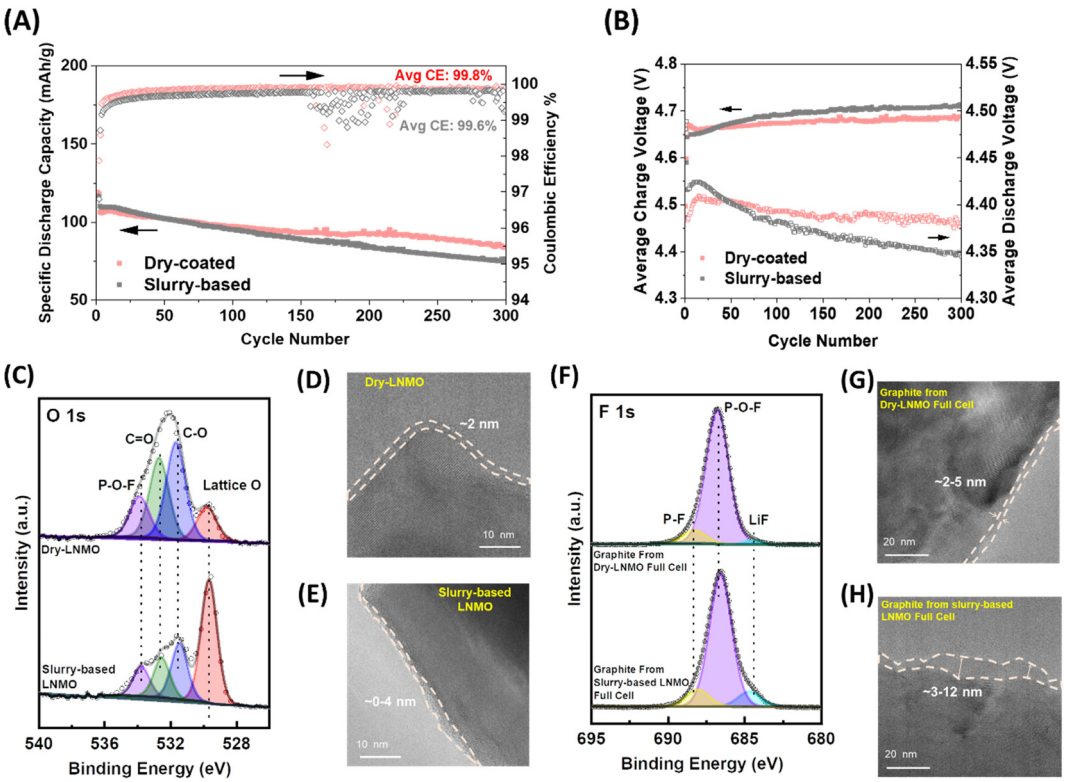

Fig. 4 Electrochemical performance and interfacial analysis between the dry-LNMO and slurry-based LNMO thick electrode full cells: (A) cycling performance with coulombic efficiencies; (B) corresponding average charge and discharge voltages; (C) XPS spectra of the O 1s region of cycled LNMO; TEM images of the surface and/or the CEI region of (D) dry-LNMO and (E) slurry-based LNMO after cycling; and (F) XPS spectra of the F 1s region of cycled graphite. TEM images of the surface and/or the SEI region of graphite cycled in (G) dry-LNMO and (H) slurry-based LNMO full cells.

Also, the reductive peaks move towards the lower voltage end. In contrast, both oxidative and reductive peak positions from the dry-LNMO full cell show limited or nearly no shift. These results suggest that a drastic impedance increase and severe Li inventory loss occurred in the slurry-based LNMO full cell. This analysis is enhanced by electrochemical impedance spectroscopy (EIS) measurements (Fig. S15C and S16, ESI†). Moreover, it was also found that after cell disassembling, the adhesion between dry-LNMO and the current collector was well maintained while slurry-based LNMO had delaminated from the Al foil (Fig. S17, ESI†). Such contact loss, possibly due to the corrosion of parasitic reaction products on the current collector or to the weaker adhesion force illustrated in Fig. 2E, will further exacerbate the cell impedance growth.

To better understand the impact of interphase properties, we characterized the CEI/SEI products from electrodes after 300 cycles using X-ray photoelectron spectroscopy (XPS). From the O 1s spectra (Fig. 4C), the intensity of lattice oxygen peak (529.9 eV) in the cycled slurry-based LNMO is much higher than that in the cycled dry-LNMO. This implies that the CEI of slurry-based LNMO is not well formed to fully cover the LNMO surface, as illustrated in Fig. 4D, with large variations in the thickness including some areas where no CEI is observed. In contrast, the dry-LNMO particle surface is protected with a conformal 2 nm thick CEI layer. Notably different CEI properties in slurry-based LNMO could be attributed to more significant attack by HF[37] triggered by the higher specific area conductive carbon electrolyte decomposition. The trace amount of H_2O from the electrolyte and from the carbonate solvent decomposition will react with PF_5, which is the major salt decomposition product, to form strongly acidic HF which will further corrode the CEI and SEI. The absence of a CEI layer on the slurry-based LNMO surface will lead to more HF corrosion on the particle surface, followed by the increasing dissolution of transition metal (TM) from the cathode and its redeposition on the graphite (Fig. S18, ESI†). The dissolution of TM cations to the electrolyte and deposition on the graphite will cause graphite poisoning, which ultimately leads to fast capacity decay.[38] The XPS results of cycled graphite anodes (Fig. 4F) further demonstrate the impact of the interphase. In the F 1s spectra, the Li–F peak intensity from graphite cycled in the slurry-based LNMO full cell is significantly higher than that of the dry-LNMO full cell. LiF is well-known as the decomposition product of the $LiPF_6$ salt.[39] This indicates that more salt decomposition is triggered in the slurry-based LNMO full cell during cycling. Moreover, the HRTEM results of the cycled graphite anode (Fig. 4G and H) also show that a much thicker layer of the SEI is formed on the surface of graphite cycled in the slurry-based LNMO full cell. This observation could suggest that more Li inventories are continuously consumed in the accelerated side reactions triggered by conductive carbon with a higher specific surface area.

Despite the surface TM dissolution observed, no bulk phase change is found in both types of cycled LNMO electrodes based on the capillary XRD results (Fig. S19, ESI†). The clear (1 1 1) peak shift indicates the loss of lithium inventories in the bulk structure. Note that the loss of Li in the bulk structure is only part of the lithium inventory loss in the full cell. Even though there is ~12% capacity retention difference in cycling performance between dry-coated and slurry-based LNMO full cells, the right shift of the (1 1 1) peak is similar in both cathodes. Thus, the major lithium inventory loss does not happen in the bulk structure, but more in the interphase formation triggered by the continuous HF corrosion on both CEI and SEI. In addition, it is also found that PTFE is coated on the carbon fiber during electrode formation. Such an insulating coating further prevents the electrolyte decomposition on the carbon active sites while allowing fast electron flows within the electrode structure (Fig. S20, ESI†).

Enhanced long-term cycling performance

With the knowledge gained from the above sections, cells were fabricated to investigate long-term cycling performance up to 1000 cycles at similar loading. Even with a commercialized carbonate-based electrolyte, our designed dry-LNMO full cell shows a capacity retention of 60% and an average Coulombic efficiency of 99.88% after 1000 cycles at a C/3 rate (Fig. 5A and B). To move one step further, one type of all-fluorinated electrolyte 1 M $LiPF_6$ in FEC : FEMC = 3 : 7 wt% was applied. The fluorination of solvent molecules aims to improve the reaction barriers and energies for the electrolyte/cathode decomposition reactions to further mitigate the parasitic reactions. Similar types of electrolytes have also been reported in previous research.[40,41] It can be found that both cycling performance and coulombic efficiency are largely improved to 68% and 99.96%, respectively, after 1000 cycles. A comparison of cell cycling performance between our results and literature reports using both the carbonate-based baseline electrolyte and novel modifications is displayed in Fig. 5D and E with detailed information listed in Tables S6 and S7 (ESI†). While most of the previous works show less than 300 cycles, several papers do report more than 300 cycles or higher than 80% capacity retention, albeit with cathode loadings less than 15 mg cm^{-2}. Elevated temperature cycling is always a challenge for Mn-base cathode materials. Under such aggressive conditions, the dry electrode with an FEC-FEMC based electrolyte can also deliver a capacity retention of ~70% after 100 cycles whereas most literature work was focused on low loading and half cells (Fig. 5C and F).[42–46] Consistent with room temperature cycling, the dry-LNMO full cells still outperform the slurry-based LNMO full cells under elevated temperature conditions. Our work has not only achieved stable long-term cycling after 1000 cycles, but more importantly, the loading has reached the commercial standard.

The pronounced cycling stability is ascribed to the combined factors of robust mechanical properties, a highly distributed and interconnected electronic percolation network, and reduced parasitic reactions (Fig. 6). In the dry electrode, strong binding force enabled by the fibrillated PTFE binder helps to maintain the close contact of various electrode components, which will reduce the cell impedance during cycling. Such a binding force is insufficient in the slurry-based electrode especially at a large thickness (~150 μm), which will lead to electrode cracks and failure. In addition, the use of carbon fiber

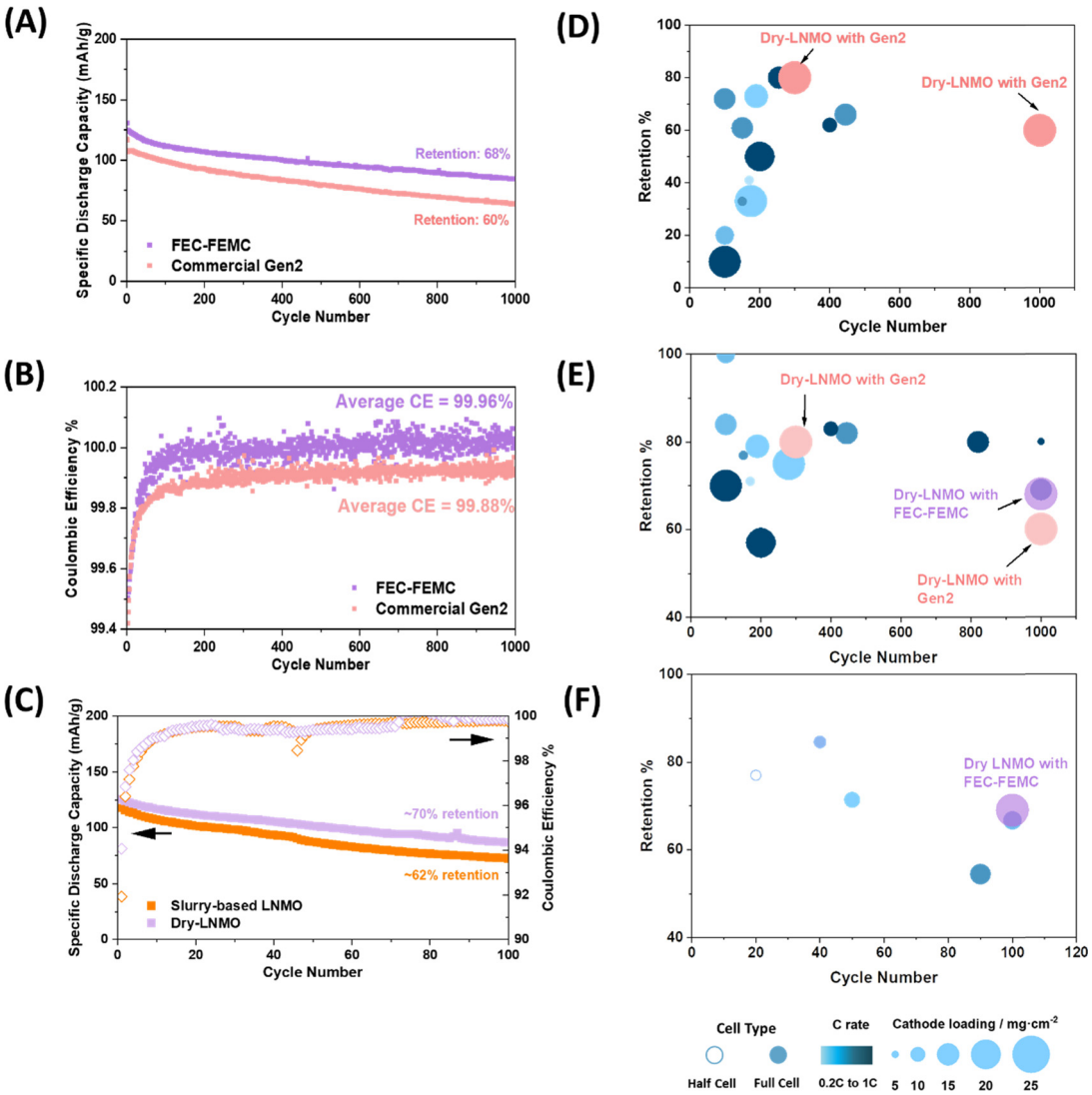

Fig. 5 Long-term cycling performance of dry-LNMO full cells with different electrolytes, (A) Specific capacity and (B) coulombic efficiency of dry-LNMO full cells using both Gen2 and FEC-FEMC based electrolytes. (C) Cycling performance of slurry-based and dry-LNMO full cells at 55 °C. Literature summary of LNMO full cell cycling performance using (D) baseline setups, (E) novel modifications and (F) at high temperature.

can effectively link a number of cathode particles to facilitate fast electron transfer and form an electronic percolation network. Meanwhile, carbon fibers with a low surface area reduce active sites for electrolyte oxidation, which will cause continuous water and HF acid generation to damage both the cathode surface and CEI layer.[47] Other than side reaction mitigation, both VGCF and the fibrillated PTFE binder show a similar fiber-shape morphology. Therefore, there will be a synergistic effect between the carbon and binder to form a partial PTFE coating onto the carbon fibers (Fig. S20, ESI†). Since PTFE is electronically insulative, it will serve as a protective coating to further prevent electrolyte oxidation at high voltage. This partial PTFE coating found on the carbon fiber can further reduce the active sites without affecting electron transfer.

The advantages achieved in dry electrodes are highly dependent on the appropriate morphology of both conductive carbon and active materials. With a similar degree of binder fibrillation, active materials with a high surface area (*e.g.* less than 1 μm particle size) may diminish the effective binder amount per unit area. This will lead to poor cohesion strength of the electrode and finally result in fabrication failure. As for conductive carbon with a low specific surface area, the ability to well connect active material particles depends on the morphological change during fabrication. As seen from our PFIB-SEM results, agglomerated VGCF was "straightened" during shear mixing, allowing the fibers to well connect to a number of LNMO particles and hence building a homogeneous electronic percolation network. Additionally, structural enhancements attributed to the synergy of PTFE and VGCF lead to electronic conductivity improvements for ultra-thick dry-coated electrodes. Finally, it is vital that a carbon-free but surface-porous current collector is used to remove the extra source of electrolyte decomposition at high voltage. The porous surface of the current collector also provides vacancies for particles to

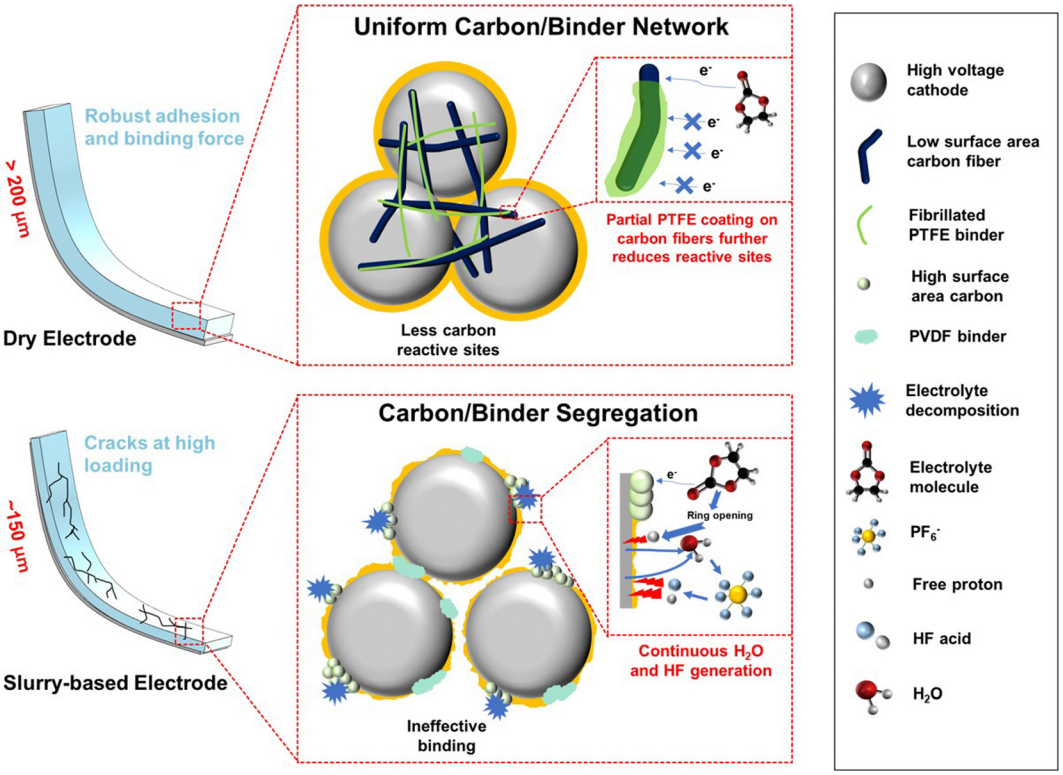

Fig. 6 Schematic of advantages achieved by the dry electrode. Utilization of a low-surface area carbon fiber to reduce side reactions while maintaining robust mechanical strength and an excellent electronic percolation network can be achieved simultaneously in the dry-coated thick electrode.

adhere into the foil during calendaring, therefore strengthening the adhesion.

Conclusions

In this work, we developed a PTFE-based dry electrode fabrication method to prepare high voltage spinel oxide LNMO electrodes. Overcoming major limitations with slurry-coated electrodes, this process enables ultra-high loadings ($\sim$68 mg cm^{-2} and $\sim$240 μm) and excellent cycling stability using a 3.0 mA h cm^{-2} level ($\sim$21 mg cm^{-2} and $\sim$90 μm) electrode at 1000 cycles with both the baseline and a high-performance fluorinated electrolyte (68% capacity retention after 1000 cycles for the full cell). Based on insights gleaned from the PFIB-SEM images and the 2D-model, further optimization of this process will likely bring opportunities to fabricate dry electrodes with an even lower amount of conductive carbon and binder, thereby improving volumetric energy density. Looking forward, this methodology can also be applied to other cathode materials operating at voltages higher than 4.5 V (*e.g.*, Li-rich layer oxides, $LiCoMnO_4$, olivine $LiCoPO_4$, high voltage LCO and NCM) leveraging low surface area conductive carbon with an appropriate morphology to form effective electronic percolation networks, particularly in highly loaded electrodes. These considerations confirm that the dry electrode method offers a promising electrode manufacturing solution which is more cost effective, environmentally benign, and sustainable.

Author contributions

W. Y., M. Z., and Y. S. M. designed the experiments. D. J. K. chose the appropriate PTFE binder for these experiments and provided PTFE technical content for the manuscript. W. Y. conducted electrode fabrication, electrochemistry testing, SEM-EDX and all data analyses. M. C. conducted the modeling and analysis. Z. L. and L. L. conducted PFIB. W. L. and W. Y. conducted XPS measurements. A. X. C., D. J. L., W. Y. and B. Sr. conducted the mechanical testing and analyzed the results. S. B. conducted HRTEM experiments and analysis. R. S. conducted the ICP measurement. B. S. conducted XRD experiments. M. A. S. helped with high performance electrolyte screening and manuscript editing. Y.-T. C. and D. H. S. T. participated in the scientific and figure discussion. G. R. conducted Physical adsorption of nitrogen at the liquid nitrogen temperature testing. W. Y. conducted XPS, XRD, PFIB, and ICP data analysis. Y. S. M. and M. Z. supervised the research. W. Y., M. Z., and M. C. wrote the manuscript. B. G., C. K. W. and A. S. conducted SEM experiments and did microstructural analysis at Chemours elucidating the fibrous structure of PTFE/VGCF conducting features. All authors contributed to the discussion and provided feedback on the manuscript.

Conflicts of interest

The authors declare no competing interests.

Acknowledgements

This work was supported by the Chemours Company. The cathode material in this work was supported by the U.S. Department of Energy's Office of Energy Efficiency and Renewable Energy (EERE) and U.S. Army Tank & Automotive Research Development and Engineering Command (TARDEC) under the award number: DEEE0008442. The SEM-EDX and HRTEM in this work were performed in part at the San Diego Nanotechnology Infrastructure (SDNI) of UCSD, a member of the National Nanotechnology Coordinated Infrastructure, which is supported by the National Science Foundation (Grant ECCS-1542148). A. X. C. and D. J. L. acknowledge support from the Air Force Office of Scientific Research (AFOSR) grant no. FA9550-22-1-0454. A. X. C. acknowledges support from the UC San Diego President's Dissertation Year Fellowship. The PFIB in this work was performed in The Thermo Fisher Scientific Americas NanoPort electron microscopy facility (located in Hillsboro, Oregon). The XPS in this work was performed at the UC Irvine Materials Research Institute (IMRI). The ICP-MS, XRD and physical adsorption of nitrogen at the liquid nitrogen temperature testing in this work were conducted at Environmental and Complex Analysis Laboratory (ECAL) in the Chemistry and Biochemistry department in UC San Diego. The authors thank Neware Instruments for the Neware battery test system. The authors are grateful for Chemours providing the PTFE binder used in the research. The authors thank Prof. Zhaoping Liu's group from Ningbo Institute of Materials Technology & Engineering (NIMTE) for providing the graphite anode.

References

1 London Metal Exchange **https://www.lme.com/en/metals/ev/lme-cobalt#Price+graphs** September 2022.
2 C. Banza Lubaba Nkulu, L. Casas, V. Haufroid, T. De Putter, N. D. Saenen, T. Kayembe-Kitenge, P. Musa Obadia, D. Kyanika Wa Mukoma, J. M. Lunda Ilunga, T. S. Nawrot and O. Luboya Numbi, *Nat. Sustainability*, 2018, **1**(9), 495–504.
3 T. Yoon, J. Soon, T. J. Lee, J. H. Ryu and S. M. Oh, *J. Power Sources*, 2021, **503**, 230051.
4 X. He, C. Du, B. Shen, C. Chen, X. Xu, Y. Wang, P. Zuo, Y. Ma, X. Cheng and G. Yin, *Electrochim. Acta*, 2017, **236**, 273–279.
5 S. H. Jung, D. H. Kim, P. Brüner, H. Lee, H. J. Hah, S. K. Kim and Y. S. Jung, *Electrochim. Acta*, 2017, **232**, 236–243.
6 B. Shen, P. Zuo, Q. Li, X. He, G. Yin, Y. Ma, X. Cheng, C. Du and Y. Gao, Lithium cobalt oxides functionalized by conductive Al-doped ZnO coating as cathode for high-performance lithium ion batteries, *Electrochim. Acta*, 2017, **224**, 96–104.
7 J. Kasnatscheew, U. Rodehorst, B. Streipert, S. Wiemers-Meyer, R. Jakelski, R. Wagner, I. C. Laskovic and M. Winter, *J. Electrochem. Soc.*, 2016, **163**(14), A2943.
8 M. S. Milien, H. Beyer, W. Beichel, P. Klose, H. A. Gasteiger, B. L. Lucht and I. Krossing, *J. Electrochem. Soc.*, 2018, **165**(11), A2569.
9 Y. M. Song, J. G. Han, S. Park, K. T. Lee and N. S. Choi, *J. Mater. Chem. A*, 2014, **2**(25), 9506–9513.
10 A. Hofmann, A. Höweling, N. Bohn, M. Müller, J. R. Binder and T. Hanemann, *ChemElectroChem*, 2019, **6**(20), 5255–5263.
11 Y. Li, G. M. Veith, K. L. Browning, J. Chen and D. K. Hensley, *Nano Energy*, 2017, **40**, 9–19.
12 T. J. Lee, J. B. Lee, T. Yoon, D. Kim, O. B. Chae, J. Jung, J. Soon, J. H. Ryu, J. J. Kim and S. M. Oh, *J. Electrochem. Soc.*, 2016, **163**(6), A898.
13 H. Lee, S. Choi, S. Choi, H. J. Kim, Y. Choi, S. Yoon and J. J. Cho, *Electrochem. Commun.*, 2007, **9**(4), 801–806.
14 C. K. Kim, K. Kim, K. Shin, J. J. Woo, S. Kim, S. Y. Hong and N. S. Choi, *ACS Appl. Mater. Interfaces*, 2017, **9**(50), 44161–44172.
15 Z. Wang, D. Cao, L. Wen, R. Xu, M. Obergfell, Y. Mi, Z. Zhan, N. Nasori, J. Demsar and Y. Lei, *Nat. commun.*, 2016, **7**(1), 1–8.
16 J. H. Kim, N. P. Pieczonka, P. Lu, Z. Liu, R. Qiao, W. Yang, M. M. Tessema, Y. K. Sun and B. R. Powell, *Adv. Mater. Interfaces*, 2015, **2**(10), 1500109.
17 G. Gabrielli, P. Axmann, T. Diemant, R. J. Behm and M. Wohlfahrt-Mehrens, *ChemSusChem*, 2016, **9**(13), 1670–1679.
18 W. Li, D. Cheng, R. Shimizu, Y. Li, W. Yao, G. Raghavendran, M. Zhang and Y. S. Meng, *Energy Storage Mater.*, 2022, **49**, 77–84.
19 U. Nisar, N. Muralidharan, R. Essehli, R. Amin and I. Belharouak, *Energy Storage Mater.*, 2021, **38**, 309–328.
20 Y. Liu, R. Zhang, J. Wang and Y. Wang, *iScience*, 2021, **24**(4), 102332.
21 J. M. Kim, C. H. Park, Q. Wu and S. Y. Lee, *Adv. Energy Mater.*, 2016, **6**(2), 1501594.
22 C. Arbizzani, F. De Giorgio and M. Mastragostino, *J. Power Sources*, 2014, **266**, 170–174.
23 D. Fan, D. Lu, S. Wu, R. Zeng, J. He, D. Shu and Y. Cai, *J. Phys. Chem. C*, 2020, **124**(15), 8057–8066.
24 C. J. Bae, C. K. Erdonmez, J. W. Halloran and Y. M. Chiang, *Adv. mater.*, 2013, **25**(9), 1254–1258.
25 S. H. Park, P. J. King, R. Tian, C. S. Boland, J. Coelho, C. J. Zhang, P. McBean, N. McEvoy, M. P. Kremer, D. Daly and J. N. Coleman, *Nat. Energy*, 2019, **4**(7), 560–567.
26 L. Ibing, T. Gallasch, P. Schneider, P. Niehoff, A. Hintennach, M. Winter and F. M. Schappacher, *J. Power Sources*, 2019, **423**, 183–191.
27 R. Sliz, J. Valikangas, H. Silva Santos, P. Vilmi, L. Rieppo, T. Hu, U. Lassi and T. Fabritius, *ACS Appl. Energy Mater.*, 2022, **5**(4), 4047–4058.
28 H. Chen, M. Ling, L. Hencz, H. Y. Ling, G. Li, Z. Lin, G. Liu and S. Zhang, *Chem. Rev.*, 2018, **118**(18), 8936–8982.
29 D. L. Wood, J. D. Quass, J. Li, S. Ahmed, D. Ventola and C. Daniel, *et al.*, *Drying Technol.*, 2018, **36**(2), 234–244.
30 C. C. Liang, M. Elizabeth Bolster and R. M. Murphy, *Metal Oxide Composite Cathode for High Energy Density Battery*, US4310609, 1979.

31 H. Duong, J. Shin and Y. Yudi, *48th Power Sources Conference*, Denver, Colorado, June 11–14, 2018.
32 E. Musk, *Tesla battery day* 2020, Tesla, Fremont, CA, USA, Sep. 22, 2020.
33 Y. Lu, C. Z. Zhao, H. Yuan, J. K. Hu, J. Q. Huang and Q. Zhang, *Matter*, 2022, **5**(3), 876–898.
34 Y. Kato, S. Shiotani, K. Morita, K. Suzuki, M. Hirayama and R. Kanno, *J. Phys. Chem. Lett.*, 2018, **9**(3), 607–613.
35 L. S. Kremer, A. Hoffmann, T. Danner, S. Hein, B. Prifling, D. Westhoff, C. Dreer, A. Latz, V. Schmidt and M. Wohlfahrt-Mehrens, *Energy Technol.*, 2020, **8**(2), 1900167.
36 Y. Li, Y. Wu, Z. Wang, J. Xu, T. Ma, L. Chen, H. Li and F. Wu, *Mater. Today*, 2022, **55**, 92–109.
37 S. Park, S. Y. Jeong, T. K. Lee, M. W. Park, H. Y. Lim, J. Sung, J. Cho, S. K. Kwak, S. Y. Hong and N. S. Choi, *Nat. commun.*, 2021, **12**(1), 1–12.
38 C. Zhan, T. Wu, J. Lu and K. Amine, *Energy Environ. Sci.*, 2018, **11**(2), 243–257.
39 S. Kim, M. Kim, I. Choi and J. J. Kim, *J. Power Sources*, 2016, **336**, 316–324.
40 C. C. Su, M. He, R. Amine, T. Rojas, L. Cheng, A. T. Ngo and K. Amine, *Energy Environ. Sci.*, 2019, **12**(4), 1249–1254.
41 X. Fan, L. Chen, O. Borodin, X. Ji, J. Chen, S. Hou, T. Deng, J. Zheng, C. Yang, S. C. Liou and K. Amine, *Nat. Nanotechnol.*, 2018, **13**(8), 715–722.
42 J. Alvarado, M. A. Schroeder, M. Zhang, O. Borodin, E. Gobrogge, M. Olguin, M. S. Ding, M. Gobet, S. Greenbaum, Y. S. Meng and K. Xu, *Mater. Today*, 2018, **21**(4), 341–353.
43 L. Hu, Z. Zhang and K. Amine, *Electrochem. Commun.*, 2013, **35**, 76–79.
44 B. Aktekin, M. J. Lacey, T. Nordh, R. Younesi, C. Tengstedt, W. Zipprich, D. Brandell and K. Edström, *J. Phys. Chem. C*, 2018, **122**(21), 11234–11248.
45 B. Aktekin, F. Massel, M. Ahmadi, M. Valvo, M. Hahlin, W. Zipprich, F. Marzano, L. Duda, R. Younesi, K. Edström and D. Brandell, *ACS Appl. Energy Mater.*, 2020, **3**(6), 6001–6013.
46 A. Kraytsberg, H. Drezner, M. Auinat, A. Shapira, N. Solomatin, P. Axmann, M. Wohlfahrt-Mehrens and Y. Ein-Eli, *ChemNanoMat*, 2015, **1**(8), 577–585.
47 Y. Li, W. Li, S. Ryosuke, D. Cheng, H. Nguyen, J. Paulsen, S. Kumakura, M. Zhang and Y. S. Meng, *Adv. Energy Mater.*, 2022, **12**(11), 2103033.

